THE UNIVERSITY of EDINBURGH

Edinburgh Research Explorer

A wafer mapping technique for residual stress in surface micromachined films

Citation for published version:
Schiavone, G, Murray, J, Smith, S, Desmulliez, MPY, Mount, A & Walton, A 2016, 'A wafer mapping technique for residual stress in surface micromachined films' Journal of Micromechanics and Microengineering. DOI: 10.1088/0960-1317/26/9/095013

Digital Object Identifier (DOI):
10.1088/0960-1317/26/9/095013

Link:
Link to publication record in Edinburgh Research Explorer

Document Version:
Publisher's PDF, also known as Version of record

Published In:
Journal of Micromechanics and Microengineering

General rights
Copyright for the publications made accessible via the Edinburgh Research Explorer is retained by the author(s) and / or other copyright owners and it is a condition of accessing these publications that users recognise and abide by the legal requirements associated with these rights.

Take down policy
The University of Edinburgh has made every reasonable effort to ensure that Edinburgh Research Explorer content complies with UK legislation. If you believe that the public display of this file breaches copyright please contact openaccess@ed.ac.uk providing details, and we will remove access to the work immediately and investigate your claim.

OPEN ACCESS

Download date: 05. Apr. 2019

IOPscience iopscience.iop.org

Home Search Collections Journals About Contact us My IOPscience

A wafer mapping technique for residual stress in surface micromachined films

This content has been downloaded from IOPscience. Please scroll down to see the full text.

2016 J. Micromech. Microeng. 26 095013

(http://iopscience.iop.org/0960-1317/26/9/095013)

View the table of contents for this issue, or go to the journal homepage for more

Download details:

IP Address: 176.27.130.111
This content was downloaded on 09/02/2017 at 19:10

Please note that terms and conditions apply.

You may also be interested in:

Young's modulus measurement of thin-film materials using micro-cantilevers
G J McShane, M Boutchich, A Srikantha Phani et al.

Design, modeling, fabrication and testing of a high aspect ratio electrostatic torsional MEMS micromirror
Kurt Joudrey, George G Adams and Nicol E McGruer

A simple analytical method for residual stress measurement on suspended MEM structures using surface profilometry
V Mulloni, S Colpo, A Faes et al.

Modeling and experimental verification of thermally induced residual stress in RF-MEMS
Aurelio Somà and Muhammad Mubasher Saleem

Doped polycrystalline 3C-SiC films with low stress for MEMS: part II. Characterization using micromachined structures
Jacob Trevino, Xiao-An Fu, Mehran Mehregany et al.

Investigating thin film stresses in stacked silicon dioxide/silicon nitride structures
Omar Zohni, Gregory Buckner, Taeyun Kim et al.

Residual stress measurement method in MEMS microbeams by using frequency shift data
Aurelio Somà and Alberto Ballestra

An equation-based nonlinear model for non-flat MEMS fixed–fixed beams with non-vertical anchoring supports
Juan Zeng, Anurag Garg, Andrew Kovacs et al.

OPEN ACCESS
IOP Publishing
Journal of Micromechanics and Microengineering
J. Micromech. Microeng. **26** (2016) 095013 (12pp)
doi:10.1088/0960-1317/26/9/095013

A wafer mapping technique for residual stress in surface micromachined films

G Schiavone[1,4], J Murray[1], S Smith[1], M P Y Desmulliez[2], A R Mount[3] and A J Walton[1]

[1] Scottish Microelectronics Centre, School of Engineering, University of Edinburgh, Edinburgh EH9 3FF, UK
[2] School of Engineering Physical Sciences, Heriot-Watt University, Edinburgh EH14 4AS, UK
[3] School of Chemistry, University of Edinburgh, Edinburgh EH9 3JJ, UK

E-mail: giu.schiavone@gmail.com

Received 10 April 2016, revised 24 May 2016
Accepted for publication 9 June 2016
Published 20 July 2016

Abstract

The design of MEMS devices employing movable structures is crucially dependant on the mechanical behaviour of the deposited materials. It is therefore important to be able to fully characterize the micromachined films and predict with confidence the mechanical properties of patterned structures. This paper presents a characterization technique that enables the residual stress in MEMS films to be mapped at the wafer level by using microstructures released by surface micromachining. These dedicated MEMS test structures and the associated measurement techniques are used to extract localized information on the strain and Young's modulus of the film under investigation. The residual stress is then determined by numerically coupling this data with a finite element analysis of the structure. This paper illustrates the measurement routine and demonstrates it with a case study using electrochemically deposited alloys of nickel and iron, particularly prone to develop high levels of residual stress. The results show that the technique enables wafer mapping of film non-uniformities and identifies wafer-to-wafer differences. A comparison between the results obtained from the mapping technique and conventional wafer bow measurements highlights the benefits of using a procedure tailored to films that are non-uniform, patterned and surface-micromachined, as opposed to simple standard stress extraction methods. The presented technique reveals detailed information that is generally unexplored when using conventional stress extraction methods such as wafer bow measurements.

Keywords: wafer mapping, residual stress, permalloy, electrodeposition, MEMS, test structures, mechanical characterisation

(Some figures may appear in colour only in the online journal)

1. Introduction

The performance of MEMS devices is largely defined by the properties of the materials used for manufacturing. The reliable prediction of the behaviour of microfabricated structures therefore requires accurate characterisation methods. In this regard, particular interest is expressed by foundries and research groups for monitoring the development of stress in MEMS films during processing, as this can deteriorate device performance and reliability [1–3]. This work concentrates specifically on identifying wafer-scale variations of the residual stress in microfabricated films, as they can lead to non-uniform device performance and consequent yield losses [1]. Conventional wafer bow measurements used to calculate the film stress through Stoney's equation are inadequate to monitor wafer level distributions, as they only deliver a single average stress value. When non-uniformities are present in the properties of the film under investigation, such as thickness,

Original content from this work may be used under the terms of the Creative Commons Attribution 3.0 licence. Any further distribution of this work must maintain attribution to the author(s) and the title of the work, journal citation and DOI.

[4] Author to whom correspondence should be addressed.

 © 2016 IOP Publishing Ltd Printed in the UK

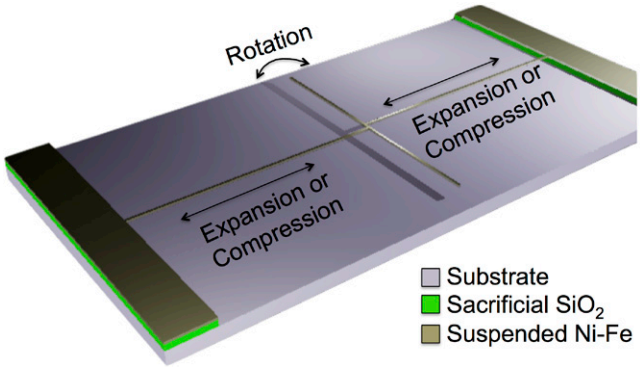

Figure 1. 3D diagram of the pointer arm microstructure used to characterize the stress in surface micromachined films.

composition and density, Stoney's formula needs complex corrections [4], and the wafer-scale calculated average stress value cannot be used as a reliable input for device design. In addition, stress distributions within patterned wafers can result in different bows along different scan diameters, thereby further complicating the extraction/calculation of the stress.

This work presents a complete procedure that enables wafer-scale mapping of the residual stress of surface micromachined layers. This is achieved by employing test structures that probe over active areas of ~2 mm^2 of deposited layers by responding to the relief of the residual stress induced by the manufacturing process. These localised measurements enable the spatial distribution of residual stress in the film under investigation to be monitored in order to identify non-uniformities and the effect of processing technology on variability. The extracted information can be used to support device design, tool qualification, and failure analysis.

The experimental demonstration of the technique presented in this work was conducted on electrochemically deposited (ECD) alloys of nickel and iron, which, due to their high magnetic permeability and low coercivity [5–7], are the main candidate materials for the microfabrication of integrated magnetic devices [8, 9]. ECD Ni–Fe alloys find application in the fabrication of MEMS devices with magnetic actuation [10–18], which offers many advantages over other schemes for MEMS actuators [19, 20]. ECD Ni–Fe alloys can exhibit large variations, the properties depending on the chemistry of the bath and the electrical parameters used for the deposition, as well as other process conditions [21–23]. The ability to optimally characterize such films during development cycles is therefore essential when new devices are being prototyped, as the measured properties can significantly differ from reported values [24–26]. Despite the favourable magnetic properties, Ni–Fe microstructures show high sensitivity to failure mechanisms induced by the relief of residual stress [27–29], which can impede the transfer of the technology to full-scale production. Hence, techniques that enable wafer-level monitoring and control of residual stress are particularly desirable for both research and commercial organisations working with magnetic film technology.

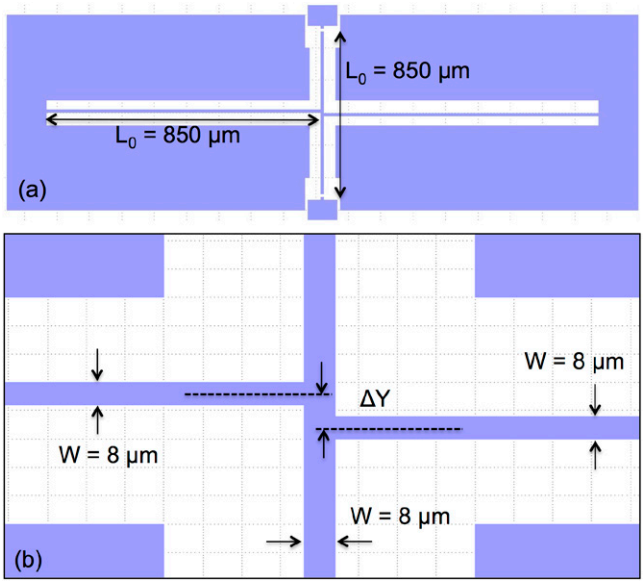

Figure 2. (a) Layout of the strain test structure with dimensions (top) and (b) magnification of the joint section (bottom).

2. Strain test sensors

This work uses previously reported rotating MEMS sensors [30–34] to obtain quantitative and localized information on the strain exhibited by suspended structures. A large number of microfabricated test structures that monitor the relief of residual stress in MEMS films have been reported in the literature, as summarized by Elbrecht *et al* [35]. The general principle of operation is to build free-standing mechanical structures where the relief of the residual stress can be visually detected. The strain sensor used for this work is a microstructure featuring a suspended pointer arm that is free to rotate when the film is subject to tensile or compressive residual stress. This test structure was preferred to buckling-type devices as in-plane strains are easier to detect and quantify optically. Figure 1 illustrates a conceptual scheme of the rotating test structure.

In this design the structures are fabricated by first depositing the layer being characterized on a sacrificial layer. The structure comprises of three elements: two parallel expansion arms and a transversal pointer arm, as shown in figure 1. The two expansion arms are anchored to the substrate at one end, while the other end is attached to the pointer arm with an offset. The structure, shown in figure 1, is patterned and the sacrificial layer is then removed to release and suspend the expansion and pointer arms, while the bigger anchor pads are still well attached to the substrate. Once released, the suspended beams, being no longer bound to the substrate, are free to contract or expand to relieve any residual stress. The extension or contraction of the expansion arms is converted into rotation of the pointer arm through the offset joint, generating a clockwise displacement in the case of tensile residual stress or a counter clockwise displacement in the case of compressive residual stress.

The rotation of the pointer arm is therefore a measure of the strain ε in the expansion arms, defined as

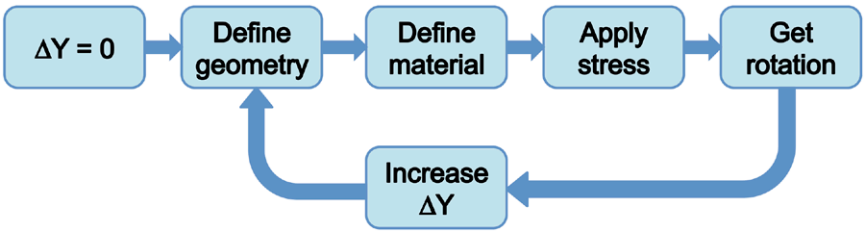

Figure 3. Simulation loop for the design of the strain sensors.

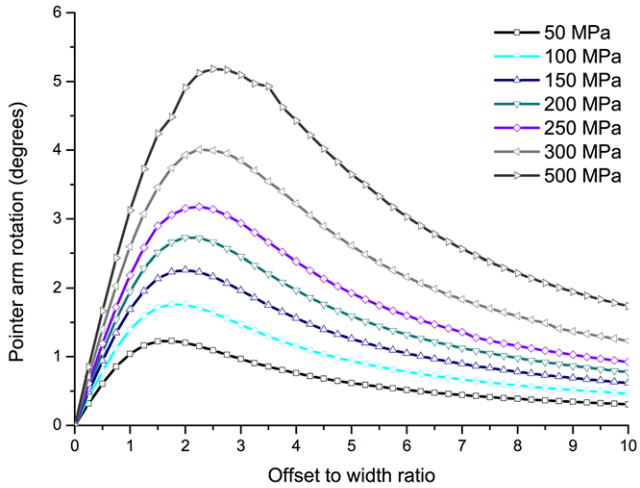

Figure 4. Pointer arm rotation as a function of the offset to width ratio $\Delta Y/W$ for various residual stress values, $W = 8\ \mu$m, and $E = 200$ GPa. Not all the curves simulated are shown.

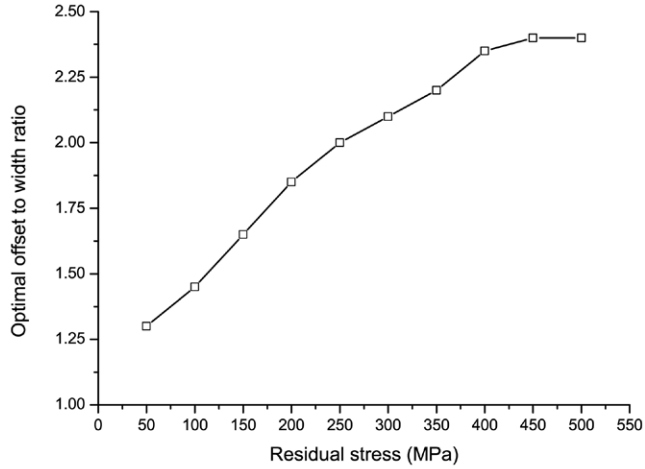

Figure 5. Optimal offset to width ratio $\Delta Y/W$ to achieve maximum rotation for various residual stress values and $E = 200$ GPa.

$$\varepsilon = \frac{\Delta L}{L_0}, \tag{1}$$

where ΔL is the change in length of the arm and L_0 is the original design length. The rotation of the arm can be optically measured to give an indication of the strain exhibited as a response to the relief of residual stress. Strain ε is related to stress σ via the relationship

$$E = \frac{\sigma}{\varepsilon}, \tag{2}$$

where E is the Young's modulus, giving an indication of the stiffness of the material. The key design point associated with this structure is to determine the optimal offset for the expansion arms joint.

2.1. Design and dimensioning

Figure 2 illustrates the generic layout of the microstructures, with the relevant dimensions highlighted. Finite element numerical analysis was employed to investigate the sensitivity of the sensor to residual stress as a function of the expansion arm offset ΔY and to assist in the sizing of devices.

The structural mechanics module of the ANSYS simulation environment was used to model the behaviour of the test structures when tensile stress is relieved through the suspended arms. This is a key calibration step in the method as the stress distribution throughout the structures is complex and difficult to model analytically. The finite element model calculates the deflection of the beams when free to relieve tensile residual stress, accounting for stress-induced stiffening effects.

Previous calculations of this type have been published that use thermal expansion to induce the strain [36]. However, in this study, a purely mechanical approach has been used, with strain calculated in response to the relief of stress. The sensitivity of the rotation to a given mechanical stress input has been determined as a function of the ratio between the expansion arm offset and beam width ($\Delta Y/W$), while keeping the expansion arm width W constant (8 μm) and using an average bulk nickel value for the Young's modulus $E = 200$ GPa. Figure 3 summarizes the simulation procedure implemented in the finite element analysis environment.

The simulation loop is used to generate a series of geometries and solve the corresponding fields for mechanical deformation. The geometric offset parameter ΔY is increased in steps of 0.25 μm, the structures redrawn accordingly, then residual stress is applied as a simulation input. The displacement field resulting from the relief of the applied stress is calculated and the rotation angle of the pointer arm extracted as sensor output.

The loop detailed in figure 3 was implemented with a scripting code that automatically solves all the defined finite element problems, generating a table of the calculated rotation angles corresponding to different mechanical stress inputs and for the specified $\Delta Y/W$ variations. The resulting relationship of the pointer arm rotation as a function of arm offset for different levels of film stress are presented in figure 4.

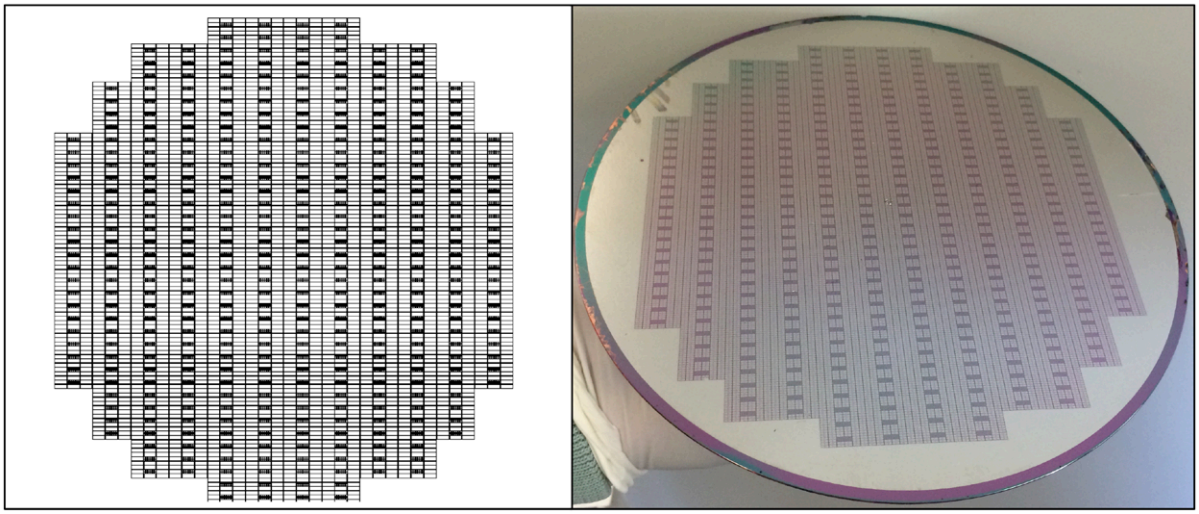

Figure 6. Floorplan of the photomask (left) and example of a processed 200 mm wafer (right). Note the edge bead where the electrical contacts are made during the ECD step.

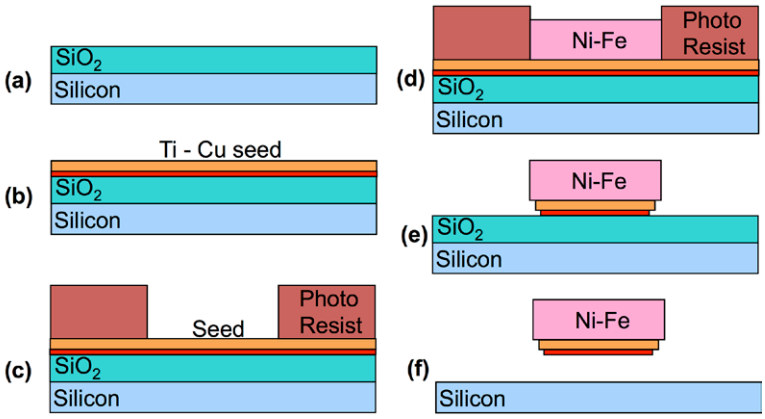

Figure 7. Fabrication process flow: cross-section through the pointer arm of the strain test structure. (a) PECVD silicon oxide deposition, (b) Ti –Cu seed layer stack sputter deposition, (c) photoresist spinning and patterning by lithography, (d) Ni–Fe electrodeposition, (e) photoresist strip and seed layer wet etch, and (f) silicon oxide vapour etch.

Table 1. Ni–Fe electroplating bath composition.

Component	Concentration (gl^{-1})
$NiCl_2 \cdot 6H_2O$	110
$FeCl_2 \cdot 4H_2O$	8
H_3BO_3	25
Saccharin	1
Na dodecyl sulphate	0.1
HCl	5

This reveals the presence of peaks of maximum sensitivity, where the rotation response to a given value of residual stress is the largest. This is expected as $\Delta Y/W$ is swept from zero, where the expansion arms are aligned and mutually counteracting, to higher values, where large offsets start to reduce the conversion of the linear deformation of the expansion into pointer arm rotation. The joint part in the centre of the sensor constitutes a mechanical load to the deformation of the expansion arms. This load is higher when the offset between the arms is small, in which case the stress is relieved partly by linear strain (producing the desired pointer arm rotation) and partly by a sideways deflection of the expansion arms. Conversely, if the offset between the arms is larger, the mechanical load is lower and the expansion arms encounter less resistance to expansion/contraction. In this case, for a given strain, the farther the expansion arms are spaced apart, the lower is the angle recorded by the pointer arm. The non-linear response curve in figure 4 is therefore explained by the superposition of these two regimes: (1) a high mechanical load part for low offset to width ratios, where the stress relief is translated in a bigger lateral deflection of the expansion arms and smaller pointer arm rotation, and (2) a small mechanical load part, where the expansion arms encounter a small resistance and for a given strain larger pointer arm rotation is recorded at lower offset to width ratios.

As a result, the sensitivity in the initial region of the curve is low as the joint is bulkier, and increases up to an optimum point, followed by a less steep decrease. The points of maximum rotation are not aligned on a single $\Delta Y/W$ value of the horizontal axis, as a consequence of non-linear stress stiffening effects. This is explicitly shown in figure 5.

It can be observed that the optimum $\Delta Y/W$ design point depends on the residual stress in the film. For electroplated Ni–Fe

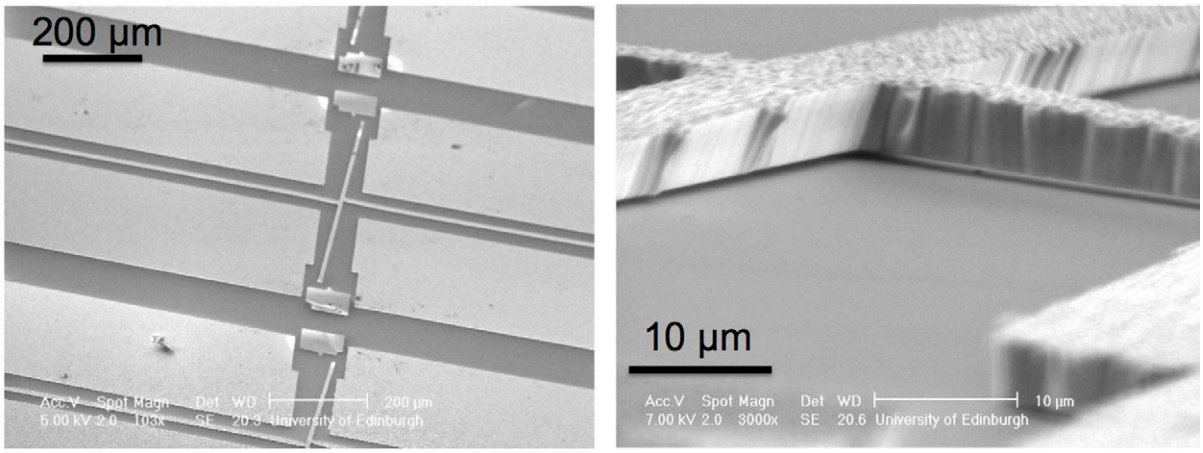

Figure 8. SEM images of manufactured strain test structures. Note the pointer arm rotation under the action of the expansion arms as the underlying seed layer has been removed.

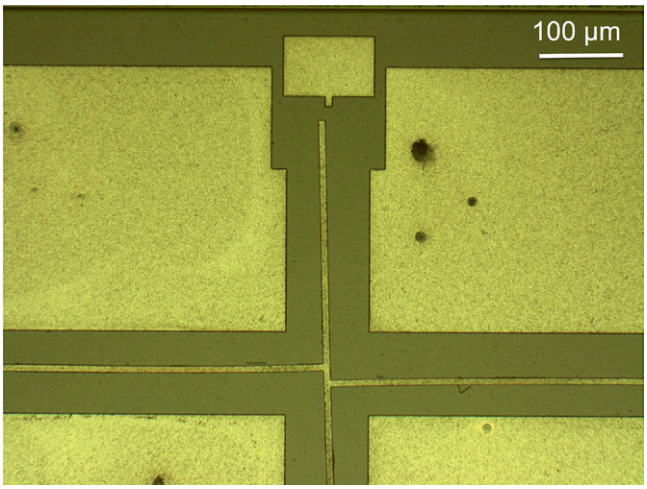

Figure 9. Fabricated Ni–Fe strain test structures exhibiting tensile stress as seen under an optical microscope after etching the sacrificial layer.

films the range of interest for the residual stress is reported to be between 100–300 MPa [37, 38], and consequently, devices with $\Delta Y/W$ ranging from 1.5 to 2 were selected. Based on the simulation results, the layout for a photomask was produced by replicating over a 200 mm diameter wafer a unit die which comprises 7 structures with $\Delta Y/W = 1.5$, 7 structures with $\Delta Y/W = 2$, and 14 structures with $\Delta Y/W = 1.75$. The number of dies on the wafer is 384, for a total of 10 752 strain test structures that cover the entire surface [23], as shown in figure 6.

Patterning by photolithography enables fine mapping across the wafer area, with a resolution limited by the size of individual strain test structures, as each sensor provides a measure of strain averaged across the active device area. Moreover, as this method uses only in-plane pointer arm strain structures, it cannot detect out-of-plane residual stress or stress gradient in the film thickness direction. Such quantities require different devices and measurement techniques, such as microcantilevers that are free to deflect in the vertical direction [39]. The sensor response calculated by FEA does not vary across devices with different thicknesses (± 0.5 μm across the wafer), as the residual stress used as simulation input is a z-extensive quantity. This means that the model is built with the assumption that the residual stress is uniformly distributed across the thickness of the film, and any stress gradient is excluded from the calculation.

2.2. Fabrication process

Test structures have been fabricated with Ni–Fe films electrodeposited on two identical 200 mm wafers. The processing steps are summarized in figure 7.

A sacrificial layer of 0.7 μm thick silicon dioxide is deposited on the silicon substrate by plasma enhanced chemical vapour deposition (PECVD), in a surface technology systems (STS) tool (figure 7(a)). A titanium and copper stack is then sputter deposited on the wafer in an OPT Plasmalab 400 magnetron sputtering system (figure 7(b)). The copper serves as seed layer for electrodeposition, and is deposited at a thickness of 300 nm to ensure good conductivity over the entire area of the wafer. The 30 nm thick titanium promotes adhesion between the copper and the underlying insulator. Photolithography is then performed to define the electroplating areas using a positive photoresist exposed using a photomask (figure 7(c)).

The electrodeposition of Ni–Fe structures is performed in a solution prepared using the components and the quantities reported in table 1, for a total volume of 35 l.

The films characterized in this work have been deposited by DC electroplating, at a current density of 20 mA cm^{-2}. This electroplating regime was selected as it reflects industrial requirement for high deposition rates.

Once the electrodeposition is completed, the photoresist is stripped and the seed stack wet etched to access the sacrificial layer for surface micromachining (figure 7(e)). Dry etch is hence performed to remove the sacrificial silicon dioxide underneath the beams and complete the release of the structures. This is performed in a Memsstar Sentry Platform (vapour HF etcher). The HF vapour etch is run until SiO_2 is completely removed from underneath the 8 μm wide beams while still anchoring the large pad areas to the substrate. Figure 8 shows SEM scans of some released test structures, while figure 9 shows an optical detail of the pointer arm rotated after stress relief.

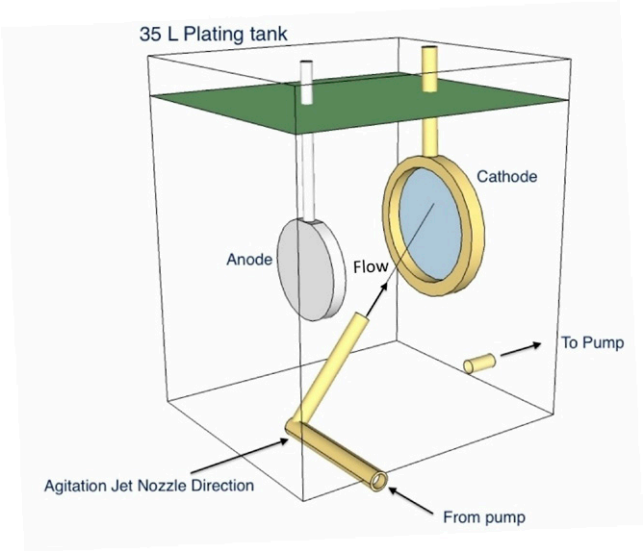

Figure 10. Diagram of the agitation system employed in the electroplating bath. The nozzle is directed towards the top of the cathode (target wafer), in order to generate non-uniformities during the deposition. The Ni–Fe film has higher Fe contents in the targeted zone.

2.3. Measurement system

The test wafer hosts 10 752 pointer arms test structures and the angle of rotation must be optically extracted from each structure to map the strain over the entire surface. A previously developed automated system [33] was therefore used, which can rapidly and reliably extract the angle of rotation from such a large number of test structures. The measurement routine consists of three major components: a camera that captures the image of the test structure, a wafer prober that scans the sample under the camera, and software that analyses the image and extracts the angle of rotation. Pattern recognition is performed using the LabVIEW Vision Assistant with an image template file being used to locate the pivot point of the pointer arms.

3. Method demonstration

Two 200 mm wafers were processed with strain test microstructures with the aim of demonstrating the stress mapping technique. These were fabricated using 5.5 μm $\pm$ 0.5 μm thick Ni–Fe electrodeposited films, which were slightly thicker around the edge of the wafer (~6 μm).

For any fabrication process the goal is to achieve uniform properties across the entire processing area. This work, however, was not targeting the minimisation of stress or its variability, but rather proving the ability to detect and display a range of stress levels and patterns across the wafer. In light of this, a source of non-uniformity was deliberately introduced during the electrodeposition process by focusing the bath agitation nozzle towards the top of the target wafer, so as to produce films that exhibit variations in alloy composition. This arrangement is illustrated in figure 10.

This particular bath arrangement has been previously shown to introduce significant variations in the alloy composition [23], with x-ray fluorescence measurements showing about 15% Fe alloy contents in the area targeted by the jet and 5% in the bottom of the wafer, with an average value of around 10%.

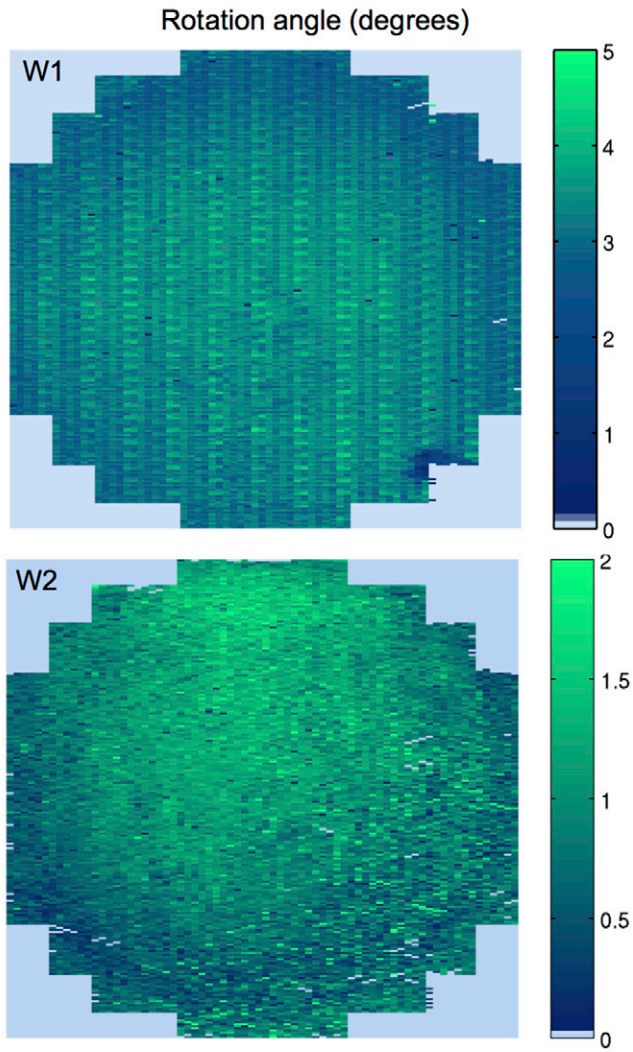

Figure 11. Maps of the measured rotation angle in degrees for W1 (top) and W2 (bottom) exhibiting tensile stress relief. Note the scale difference between the two chromatic maps.

In addition to the wafer-level non-uniformities introduced within the electrodeposition process, the second aim of the mapping method is to reveal wafer-to-wafer process differences. To this end, after electroplating and seed stripping (figure 7(e)), one of the patterned wafers, hereinafter referred to as 'W1', was heated to 150 °C for 10 min on a hot plate in air before the final HF vapour etching of the sacrificial PECVD SiO_2 layer. The second wafer, hereinafter referred to as 'W2', was instead released using the vapour etch tool directly after the seed stripping step. The same thermal treatment as W1 was then administered to W2 with the strain structures already released (figure 7(f)). Thermal treatment at the rather mild temperature of 150 °C for 10 minutes was selected as higher thermal loads introduce excessive levels of stress and oxidation in ECD Ni–Fe films [29].

3.1. Strain measurements

Figure 11 presents wafer maps measured on the rotating arm test structures of W1 and W2, which show that the angle of

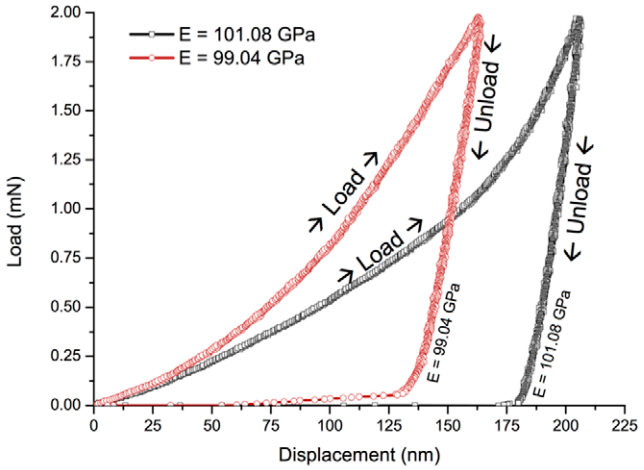

Figure 12. Example of indentation curve on the produced ECD Ni–Fe films.

rotation (strain) has clear wafer-scale non-uniformities. The chromatic patterns are similar on the two wafers, but the magnitudes of the strain are markedly different.

W1 shows significantly larger pointer arm rotation angles (2°–5°) compared to W2 (0°–2°), suggesting that the electroplated Ni–Fe film retains significantly more stress if heated before the release step. Conversely, the heat treatment administered to W2 after the release results in the pointer arms registering a lower rotation. As discussed in [23], the information extracted with this method pertains solely to the investigated Ni–Fe layer, and excludes the influence of the residual stress in the substrate and other underlying layers.

3.2. Young's modulus measurements

The strain measurements presented confirm the effectiveness of micromechanical test structures and the associated measurement system as a powerful tool for the characterisation of wafer-scale variations. However, these devices do not offer a direct reading of the residual stress, but only a local measure of the strain. It is possible to calculate the stress when the strain and Young's modulus are known, using equation (2). Unfortunately, Young's modulus values for the thin films used in MEMS technologies are dependent on the deposition and related process conditions. Using values reported in the literature is therefore not a reliable approach as the range of variation in Young's modulus for MEMS Ni–Fe films is reported between 65 and 210 GPa [37, 38, 40]. Given that the properties of electroplated films differ significantly from bulk materials, reporting consistent values is a challenging task as a huge number of parameters that describe the growth process have to be taken into consideration. In particular, the values for the Young's modulus of ECD Ni–Fe films are expected to be significantly lower than the reported bulk values because the electroplating process causes organic molecules from the bath additives as well as voids to be included in the film while it grows,

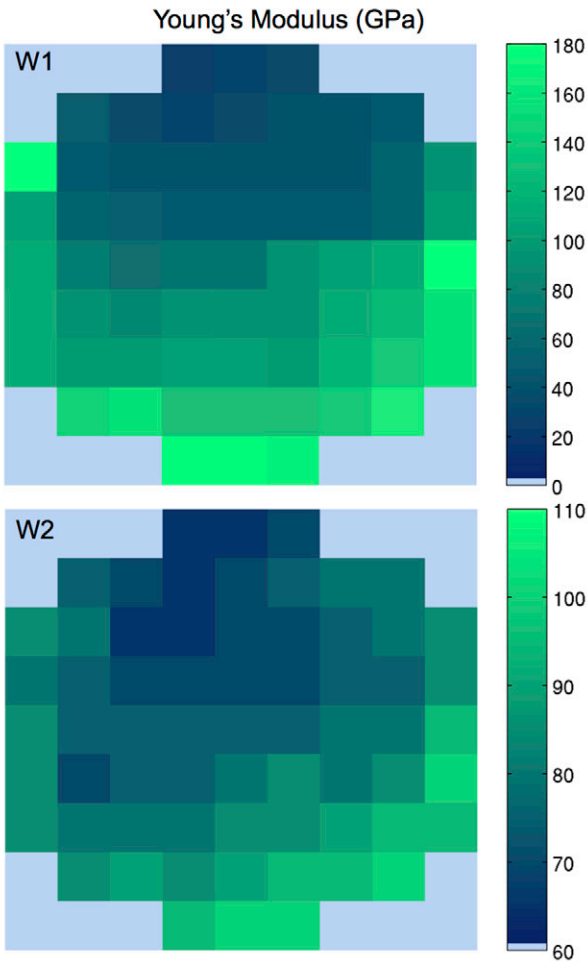

Figure 13. Maps of the measured Young's modulus in GPa for W1 (top) and W2 (bottom). Note the scale difference between the two chromatic maps.

affecting primarily the grain structure and therefore the material density [28].

Nanoindentation measurements on the patterned films have been performed to spatially determine the mechanical properties of the two ECD Ni–Fe films, with the aim of obtaining quantitative and localized stiffness information [34]. The adopted measurement method is the one introduced by Doerner and Nix [41] and refined by Oliver and Pharr [42]. In order to exclude substrate effects in the indentation measurement, the penetration depth of the tip should be negligible with respect to the thickness of the film under investigation.

The Young's modulus and the hardness of a specimen are extracted by fitting experimental load-displacement curves using the calibrated geometrical parameters of an indentation tip. It is possible to correlate the effective elastic modulus E_{eff} to the area function A, which is a measure of the cross-section of the contact as a function of the penetration depth, and to the unloading stiffness S of the indentation curve through the relationship

$$S = \beta \frac{2}{\pi} E_{\mathrm{eff}} \sqrt{A}, \tag{3}$$

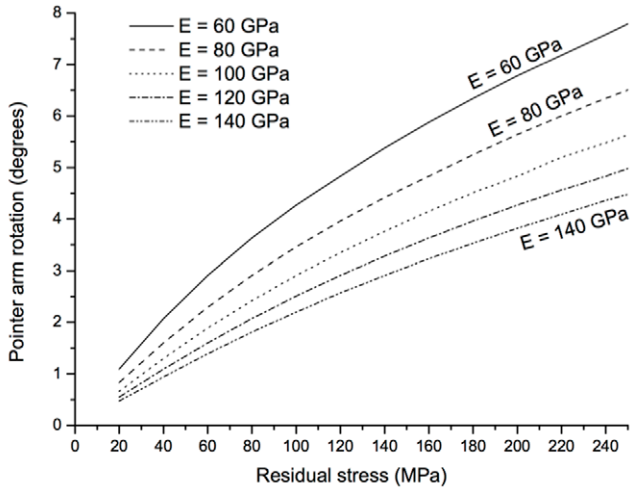

Figure 14. FEA curves simulaing the pointer arm rotation angle in response to the relief of tensile residual stress for various Young's modulus values. Note that only some of the curves are shown for ease of viewing.

where β is a dimensionless parameter used to account for the lack of axial symmetry [42]. The effective elastic modulus E_{eff} is correlated to the Young's modulus of the specimen E by

$$E_{\text{eff}} = \left(\frac{1-\nu^2}{E} + \frac{1-\nu_i^2}{E_i} \right)^{-1}, \tag{4}$$

where E_i and ν_i are the Young's modulus and the Poisson's ratio for the indenter tip as provided by the manufacturer, and ν is the Poisson's ratio of the specimen.

A Hysitron TI 900 TriboIndenter equipped with a Berkovich diamond tip has been used to perform indentation measurements and automatically extract the effective Young's modulus value on test locations that span the entire surface of wafers W1 and W2. Young's modulus values of the investigated portions of the Ni–Fe films are extracted using (4) and substituting the tip manufacturer specifications and assuming $\nu = 0.3$ [43].

A typical curve for electroplated Ni–Fe is shown in figure 12. The graph is obtained by setting a load profile that linearly ramps the force from 0 to 2 mN in 5 s and then removes the load with a downward ramp symmetrical in time with respect to the loading ramp.

Fitting of the unload portion of the curves of figure 12 reveals that the Young's modulus for this particular location in the Ni–Fe film is around 100 GPa. The above procedure has been applied to wafers W1 and W2 to produce wafer-scale maps of the Young's modulus for the two ECD Ni–Fe films.

Figure 13 shows the resulting wafer maps and the spatial distribution of Young's modulus across the entire surface of the two wafers. The maps were obtained by conducting tests at 65 positions of the wafer surface (shown as pixels in figure 13), where individual sets of nanoindentation measurements were performed. Each of the squares in figure 13 represents the average of indentation measurements taken at 4 points on the anchor areas of the electrodeposited film. As a measure of the uncertainty of these measurements, the variation within each set of 4 measurements ranged between 3 and 10%, accounting for micro-scale local variability and tool precision.

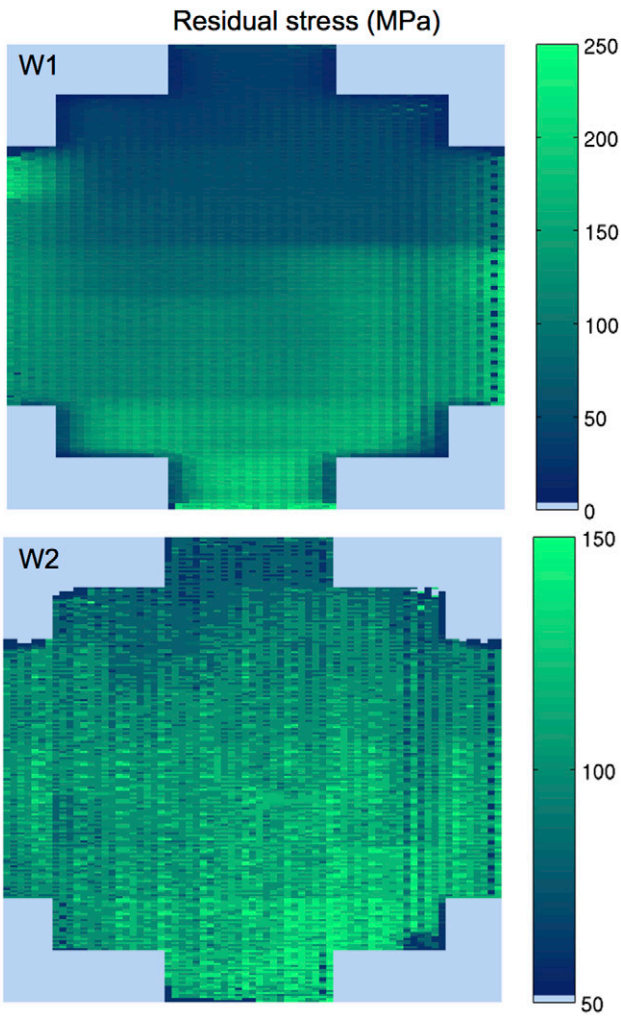

Figure 15. Maps of the extracted residual stress in MPa for W1 (top) and W2 (bottom). Note the scale difference between the two chromatic maps.

The non-uniform mechanical behaviour of the film across the wafer is due to the combined effect of a series of process parameters, such as thickness, alloy composition, density, inclusion of impurities, current density patterns, etc. The measured values for wafer W1 (top) cover a wafer-scale range from 30 to 180 GPa, exhibiting significant spatial variation. Smaller but still significant variations are observed for wafer W2 (bottom), with Young's modulus values between 60 and 110 GPa.

3.3. Extraction of residual stress

The previously obtained strain and Young's modulus measurements need to be combined to determine the residual stress. Finite element numerical analysis is used to couple the measured rotation angles with the experimental values of the Young's modulus, in order to extract the local values

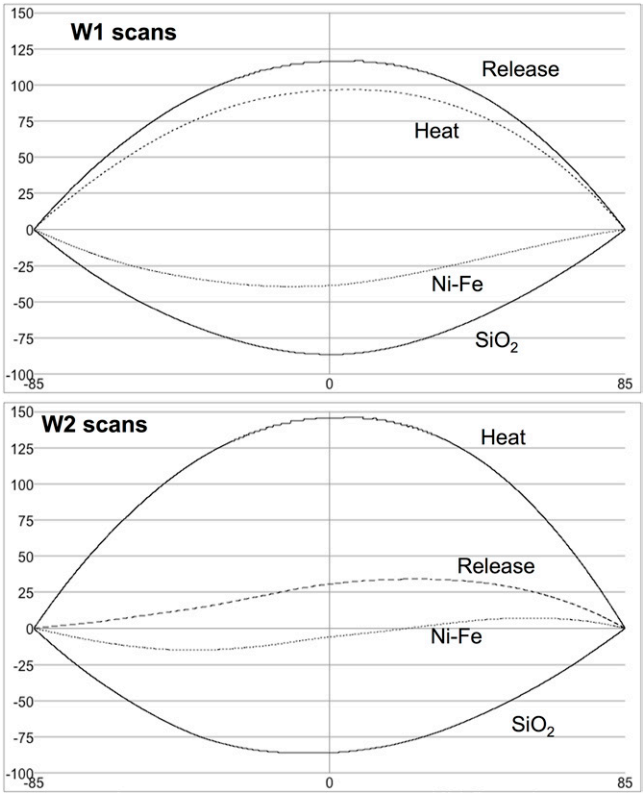

Figure 16. Wafer bow measurements at each processing step for W1 (top) and W2 (bottom). The *x*-axis represents the scan length (−85 mm to 85 mm), while the profile scan is reported in μm on the *y*-axis [23].

of residual stress. The ANSYS structural mechanics module was used to simulate the response of the fabricated test structures to stress relief in the film. A set value of tensile residual stress is defined in the material as an initial condition and the problem is then solved for strain, for a given value of Young's modulus. The simulation procedure is parameterized and automated through scripting, generating a solution matrix containing the expected rotation angles for increasing values of residual stress (20 MPa–1000 MPa, in steps of 20 MPa), for a range of Young's moduli (20 GPa–200 GPa, in steps of 5 GPa) and for the geometrical variations patterned on the test mask. Families of curves can therefore be built that express the relationship between the residual stress in the film and the angular response of the sensor, for different values of Young's modulus in the range measured via nanoindentation. Figure 14 shows a portion of the simulation plots for the pointer arm devices undergoing rotation as a response to residual tensile stress, with Young's moduli ranging between 80 and 115 GPa. For visual clarity, not all the curves are shown.

The value of the Young's modulus for each specific location (figure 13) of the electrodeposited film is associated with the corresponding set of rotation data points (figure 11). With reference to figure 14, a simulation curve is selected based on the measured Young's modulus, and a point on the vertical axis is selected based on the measured rotation. The corresponding point on the horizontal axis is the extracted value of the residual stress for the specific location considered on the wafer. The extraction procedure is automated in Matlab using

Table 2. Wafer bow measurements on W1 and W2.

Process step	Bow on W1 (μm)	Bow on W2 (μm)
SiO_2 deposition	−86.6	−86.3
Ni–Fe electroplating	−39.6	−15.1
Pre-release heating	96.9	—
Releasing	116.8	34.1
Post-release heating	—	146.2

the measurements and FE data sheets as input, allowing for the rapid construction of wafer-scale maps of the residual stress. Figure 15 shows the compiled maps of residual stress for wafers W1 and W2.

The residual stress values obtained using this approach ranged between 50 MPa and 220 MPa for wafer W1 and from 60 MPa to 150 MPa for wafer W2. It is satisfying that these residual stress levels fall within the ranges reported in the literature for similar films [37, 38]. Once again, wafer W1 shows variation on a much larger scale than wafer W2.

4. Discussion of the results

The results presented show clear patterns and differences across the surface of the two quasi-identically processed wafers. Although the previously reported rotation plots (figure 11) are very useful for monitoring the spatial distribution at the wafer level of the mechanical response to stress of the material under analysis, such measurements carry an intrinsic uncertainty. They do not identify whether the observed strain patterns are due to thermal mismatch effects, or structural changes in the Ni–Fe film during process steps affecting its mechanical properties. For instance, the residual stress could be uniformly distributed across the wafer, but the process non-uniformities may be causing the material to be locally stiffer or softer due variations in the Ni–Fe ratio, and therefore create strain patterns that do not carry any information pertaining the induced residual stress levels.

The reported set of measurements addresses this question through the ability to spatially and quantitatively wafer map the residual stress developed in micromachined materials. In the example presented in figure 15 the highest stress levels are associated with the stiffest portions of the films situated on the lower right edge of both wafers, where slightly lower rotation angles are observed.

These results suggest that previously reported strain maps are a very powerful means of monitoring and tracking local variations and changes across the wafer surface and of detecting non-uniformities related to specific process conditions. Such maps are best used however in combination with the measured Young's modulus maps, which show a much higher and significant spatial variation. This example demonstrates that stress-relief based test structures indicating strain cannot be considered alone as a direct indication of the distribution of the residual stress of the material. In the particular case of wafers W1 and W2, the measured Young's modulus variations are large enough to cause the developed residual stress

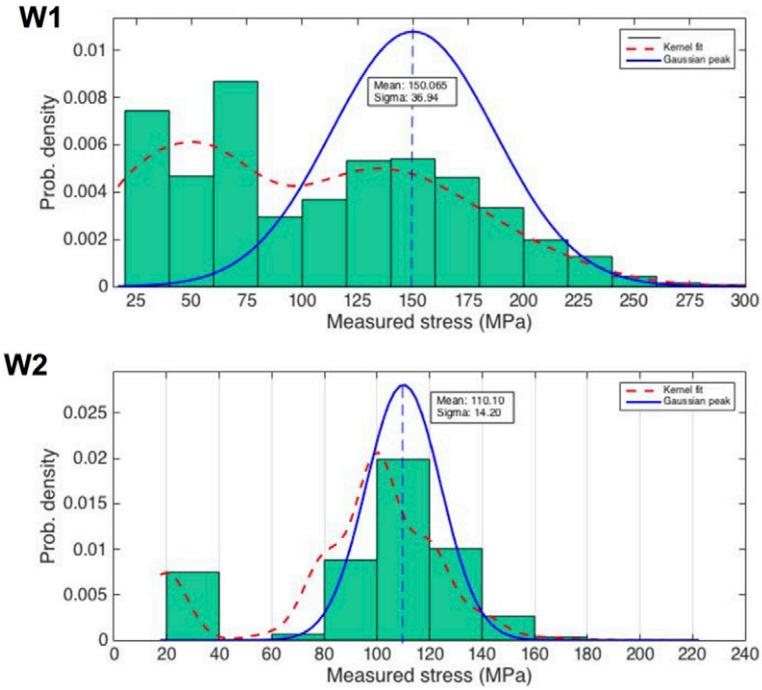

Figure 17. Statistical distribution of the experimental stress data for wafers W1 (top) and W2 (bottom). The histograms are binned at 20 MPa and Gaussian curves are used to model the high-stress peaks.

to be relieved in a fashion that cannot be extracted through simple strain detection experiments. Thus, when a film is subject to a certain distribution of residual stress, the variation of Young's modulus may represent, as in this example, a dominant contribution to the formation of the observed strain patterns, which may erroneously be deemed a direct indication of stress levels. Nonetheless, the strain test structures can be used to identify key process parameters responsible for certain observed effects or patterns, as previously seen for instance for the effect of bath agitation [23].

In this final section, a comparison between the mapping routine and the conventional wafer bow method is presented. Figure 16 shows wafer bow measurements taken on wafers W1 and W2 at different processing steps. The curves shown in figure 16 were optically measured on the back side of W1 and W2 using a Frontier Semiconductor FSM 500TC [23]. To facilitate these measurements, double-side polished wafers were used as starting substrates for W1 and W2. It should be noted that the wafer bow is a measure of the effect of all the films on the wafer and only provides a single value with no indication of any spatial variation.

In this experiment the wafer profile was scanned on both wafers after SiO_2 deposition, Ni–Fe electrodeposition, release and thermal treatment. The curves obtained are reported in figure 16, showing for both wafers an initial overall compressive stress and progressive build-up of tensile stress with each fabrication step. The measured bow values are listed in table 2[5].

[5] The bow values extracted from the scans for W2—Ni–Fe electrodeposition and W2—release cannot be considered as actual bows, as the profiles are clearly irregular.

The biggest jump in the curves is observed after the heating step, which probably results from induced structural changes in the film. The final bow measurements suggest that higher overall stress is present in W2 compared with W1. To enable an effective comparison, the experimental stress data mapped in figure 15 was analysed for both wafers, as shown in figure 17.

A simple average calculation on the data shows mean residual stress values of 90.62 MPa and 100.67 MPa for wafers W1 and W2, respectively. W2 thus exhibits on average higher stress than W1, which is consistent with the larger wafer bow measured in figure 16. Unfortunately a direct stress comparison is not possible, as the sample films used in this demonstration do not satisfy the hypotheses for the validity of Stoney's formula, conventionally applied to uniform blanket thin films [4].

Although there is a certain degree of agreement between the two measurement techniques, the mapping method provides significantly more details on the stress development in the film. For instance, both wafers exhibit two separate stress data populations, with at least two distinct peaks across the distribution. It is important to note that the resolution of the binning in this demonstration is limited by the step used to increase the input residual stress in the finite element simulations, as described in the previous sections. The dominant peaks are modelled with Gaussian fits in figure 17, showing much smaller variability in W2, with standard deviation 14.20 (12.90% relative) compared to W1, with standard deviation 36.94 (24.61% relative). This tends to suggest that the heat treatment after the release of the suspended structures compresses the range of variation of the residual stress compared to the case of heat treatment pre-release, where a broader variability is observed. However, this hypothesis needs further

experimental validation on a statistically significant number of samples, which is beyond the scope of this paper.

With regards to the precision of the presented method, the actual accuracy of each individual FE simulation has been neglected, as a greater contribution to inaccuracy is due to the step chosen for the sweep of the simulation parameters. As discussed in the previous sections, the model uses sweeps of Young's modulus and input residual stress, with steps of 5 GPa and 20 MPa respectively. These values are retained as limits to the precision of the method. Sweeps with less coarse steps can improve the precision, and the accuracy of the calculation is in this case limited by the actual simulation error.

The experimental results presented in this work demonstrate the power of the proposed mapping technique, as it allows the extraction of detailed information otherwise hidden behind the conciseness of single average values obtained with conventional bow measurements.

5. Conclusions

The results presented demonstrate a practical semi-automated wafer mapping technique that can be used to map the residual stress in microstructures released via surface micromachining. The reported application to two ECD Ni–Fe films proves the detection of both wafer-level non-uniformities and wafer-to-wafer differences resulting from process splits. A consistency was found between the mapping technique and conventional wafer bow measurements, both identifying the Ni–Fe film subject to the post-release heat treatment as the one with larger residual stress.

A higher level of detail is made available by the above mapping technique, with insights on wafer-scale and wafer-to-wafer variability with regards to stress development. This identified, for instance, that the wafer with higher average residual stress exhibits a much narrower range of variation for the residual stress. The results presented suggest that for the analysis of processing effects on residual stress at the wafer level, the wafer mapping technique is a much more suitable tool than wafer bow measurements. This method is particularly effective for the case of thin films that are non-uniform, patterned and surface micromachined, as the structural film complexity prevents the use of Stoney's formula. In the case of uniform deposition with negligible wafer-scale variability, Stoney's formula is a key tool to obtain a single average value for the residual stress. This is however not always the typical scenario in research and development, and the method presented in this paper can help benchmark the uniformity and quality of thin-film processes with regards to residual stress.

Although the technique is demonstrated on ECD Ni–Fe films and structures, it can be broadly applied to any material where stress development is of significant interest. This consideration makes this method useful for a different range of situations, such as the qualification of processes and deposition tools, failure analysis, and process windows identification.

Acknowledgments

This work was supported by the Edinburgh Research Partnership in Engineering and Mathematics, EPSRC/IeMRC through DTA funding DTA/15/2007, IeMRC/EPSRC (FS/01/02/10) through the Smart Microsystems grant. The financial support of Texas Instruments is gratefully acknowledged and the authors would like to thank Memsstar for access to their XeF_2 and HF etch tools.

Data presented in paper are available at http://dx.doi.org/10.7488/ds/1424.

References

[1] Strojwas A J 2006 Conquering process variability: a key enabler for profitable manufacturing in advanced technology nodes *Proc. IEEE Int. Symp. on Semiconductor Manufacturing (ISSM), 2006* pp xxiii–xxxii

[2] Horsfall A B *et al* 2004 Dependence of process parameters on stress generation in aluminum thin films *IEEE Trans. Device Mater. Rel.* **4** 482–7

[3] Zhang Y-H, Ding G-F, Cai Y-L, Wang H and Cai B 2006 Electroplating of low stress permalloy for MEMS *Mater. Charact.* **57** 121–6

[4] Feng X, Huang Y and Rosakis A J 2007 On the stoney formula for a thin film/substrate system with nonuniform substrate thickness *J. Appl. Mech.* **74** 1276–81

[5] Luo J K, Pritschow M, Flewitt A J, Spearing S M, Fleck N A and Milne W I 2006 Effects of process conditions on properties of electroplated Ni thin films for microsystem applications *J. Electrochem. Soc.* **153** D155–61

[6] Arai K I and Honda T 1996 Micromagnetic actuators *Robotica* **14** 477–81

[7] Niarchos D 2003 Magnetic MEMS: key issues and some applications. *Sensors Actuators* A **106** 255–62

[8] Sullivan C R and Sanders S R 1996 Design of microfabricated transformers and inductors for high-frequency power conversion *IEEE Trans. Power Electron.* **11** 228–38

[9] Daniel L, Sullivan C R and Sanders S R 1996 Design of microfabricated inductors *IEEE Trans. Power Electronics* pp 709–23

[10] Taylor W P, Brand O and Allen M G 1998 Fully integrated magnetically actuated micromachined relays *J. Microelectromech. Syst.* **7** 181–91

[11] Taylor W P and Allen M G 1997 Integrated magnetic microrelays: normally open, normally closed, and multi-pole devices *Transducers '97—Proc. Int. Conf. on Solid State Sensors and Actuators, 1997* pp 1149–52

[12] Ruan M, Shen J and Wheeler C B 2001 Latching micromagnetic relays *J. Microelectromech. Syst.* **10** 511–7

[13] Cho I-J, Song T, Baek S-H and Yoon E 2005 A low-voltage and low-power RF MEMS series and shunt switches actuated by combination of electromagnetic and electrostatic forces *IEEE Trans. Microw. Theory Tech.* **53** 2450–7

[14] Cho I-J and Yoon E 2010 Design and fabrication of a single membrane push–pull SPDT RF MEMS switch operated by electromagnetic actuation and electrostatic hold *J. Micromech. Microeng.* **20** 035028

[15] Glickman M, Tseng P, Harrison J, Niblock T, Goldberg I B and Judy J W 2011 High-performance lateral-actuating magnetic MEMS switch *J. Microelectromech. Syst.* **20** 842–51

[16] Gray G D Jr and Kohl P A 2005 Magnetically bistable actuator: part 1. Ultra-low switching energy and modeling *Sensors Actuators* A **119** 489–501

[17] Gray G D Jr, Prophet E M, Zhua L and Kohl P A 2005 Magnetically bistable actuator: part 2. Fabrication and performance *Sensors Actuators* A **119** 502–11
[18] Fu S, Ding G, Wang H, Yang Z and Feng J 2007 Design and fabrication of a magnetic bi-stable electromagnetic MEMS relay *Microelectron. J.* **38** 556–63
[19] Rebeiz G M 2003 RF MEMS switches: status of the technology *Proc. 12th Int. Conf. on Transducers, Solid-State Sensors, Actuators and Microsystems, 2003* vol 2 pp 1726–9
[20] Schiavone G, Desmulliez M P Y and Walton A J 2014 Integrated magnetic MEMS relays: status of the technology *Micromachines* **5** 622–53
[21] Koo B and Yoo B 2010 Electrodeposition of low-stress NiFe thin films from a highly acidic electrolyte *Surf. Coat. Technol.* **205** 740–4
[22] Flynn D and Desmulliez M P Y 2010 Influence of pulse reverse plating on the properties of Ni–Fe thin films *IEEE Trans. Magn.* **46** 979–85
[23] Murray J, Schiavone G, Smith S, Terry J G, Mount A R and Walton A J 2011 Characterisation of electroplated NiFe films using test structures and wafer mapped measurements *Proc. 2011 IEEE Int. Conf. on Microelectronic Test Structures (ICMTS), 2011* pp 63–8
[24] Myung N V and Nobe K 2001 Electrodeposited iron group thin-film alloys: structure-property relationships *J. Electrochem. Soc.* **148** C136–44
[25] Segmüller A 1961 Annealing behavior and temperature dependence of the magnetic properties of thin Permalloy films *J. Appl. Phys.* **32** 89S–90S
[26] Smith D O 1958 Static and dynamic behavior of thin Permalloy films *J. Appl. Phys.* **29** 264–73
[27] Girard R 1967 The electrodeposition of thin magnetic Permalloy films *J. Appl. Phys.* **38** 1423–30
[28] Hadian S E and Gabe D R 1999 Residual stresses in electrodeposits of nickel and nickel–iron alloys *Surf. Coat. Technol.* **122** 118–35
[29] Schiavone G, Bunting A S, Desmulliez M P Y and Walton A J 2014 Fabrication of electrodeposited Ni–Fe cantilevers for magnetic MEMS switch applications *J. Microelectromech. Syst.* **24** 870–9
[30] van Drieënhuizen B P, Goosen J F L, French P J and Wolffenbuttel R F 1993 Comparison of techniques for measuring both compressive and tensile stress in thin films *Sensors Actuators* A **37–8** 756–65
[31] Zhang X, Zhang T-Y and Zohar Y 1998 Measurement of residual stresses in thin films using micro-rotating structures *Thin Solid Films* **335** 97–105
[32] Murray J, Smith S, Schiavone G, Terry J G, Mount A R and Walton A J 2012 Correlation of optical and electrical test structures for characterisation of copper self-annealing *Proc. 2012 IEEE Int. Conf. on Microelectronic Test Structures (ICMTS), 2012* pp 152–8
[33] Smith S *et al* 2012 Fabrication and measurement of test structures to monitor stress in SU-8 films *IEEE Trans. Semicond. Manuf.* **25** 346–54
[34] Schiavone G, Desmulliez M P Y, Smith S, Murray J, Sirotkin E, Terry J G, Mount A R and Walton A J 2012 Quantitative wafer mapping of residual stress in electroplated NiFe films using independent strain and Young's modulus measurements *Proc. 2012 IEEE Int. Conf. on Microelectronic Test Structures (ICMTS), 2012* pp 105–10
[35] Elbrecht L, Storm U, Catanescu R and Binder J 1997 Comparison of stress measurement techniques in surface micromachining *J. Micromech. Microeng.* **7** 151–4
[36] Smith S, Brockie N L, Murray J, Wilson C J, Horsfall A B, Terry J G, Stevenson J T M, Mount A R and Walton A J 2010 Analysis of the performance of a micromechanical test structure to measure stress in thick electroplated metal films *Proc. 2010 IEEE Int. Conf. on Microelectronic Test Structures* pp 80–5
[37] Zhou Z, Zhou Y, Cao Y, Ding W and Mao H 2008 The evaluation of Young's modulus and residual stress of Cu films by NiFe/Cu bilayer film microbridge tests *J. Micromech. Microeng.* **18** 015027
[38] Zhou Z M, Zhou Y, Yang C S, Chen J A, Ding G F, Ding W, Wang M J and Zhang Y M 2004 The evaluation of Young's modulus and residual stress of nickel films by microbridge testing *Meas. Sci. Technol.* **15** 2389–94
[39] Zhang Y and Zhao Y P 2006 An effective method of determining the residual stress gradients in a micro-cantilever *Microsyst. Technol.* **12** 357–64
[40] Chung C and Allen M 1996 Measurement of mechanical properties of electroplated nickel–iron alloys *Proc. 1996 ASME Int. Mechanical Engineering Congress and Exposition (ASME), 1996*
[41] Doerner M F and Nix W D 1986 A method for interpreting the data from depth-sensing indentation instruments *J. Mater. Res.* **1** 601–9
[42] Oliver W C and Pharr G M 2004 Measurement of hardness and elastic modulus by instrumented indentation: advances in understanding and refinements to methodology *J. Mater. Res.* **19** 3–20
[43] Köster W and Franz H 1961 Poisson's ratio for metals and alloys *Metall. Rev.* **6** 1–56